Nano Research

Open Access

Research Article

Atomically precise nickel-sulfur clusters for efficient electrochemical 2,5-hydroxymethylfurfural oxidation

Fen Wang[1], Lu-Yu Liu[1], Sha-Sha Cui[1], Ting-Ting Li[1], Xiao-Meng Yang[1], Zhijuan Liu[1] ✉, and Yanyong Wang[2]

[1] *Henan Key Laboratory of Crystalline Molecular Functional Materials, Henan International Joint Laboratory of Tumor Theranostical Cluster Materials, Green Catalysis Center, and College of Chemistry, Zhengzhou University, Zhengzhou 450001, China*
[2] *State Key Laboratory of Chem/Bio-sensing and Chemometrics, College of Chemistry and Chemical Engineering, Hunan University, Changsha 410082, China*

Cite this article: *Nano Research*, **2025**, *18*, 94907018. https://doi.org/10.26599/NR.2025.94907018

ABSTRACT: Nickel sulfide exhibits excellent catalytic activity in the electrochemical 2,5-hydroxymethylfurfural oxidation reaction (HMFOR). However, due to the polydispersity of nanoparticles, it is difficult to establish a clear structure–activity relationship at the atomic level. In this work, we have successfully synthesized atomically precise $Ni_6(PET)_{12}$ and $Ni_4(PET)_8$ clusters (PET: 2-phenylethanethiol) for HMFOR. Ni^{2+} and S^{2-} with atomic ratio of 1:2 was mainly existed in $Ni_6(PET)_{12}$ and $Ni_4(PET)_8$ to form Ni–S bond. The electrochemical test results have suggested both $Ni_6(PET)_{12}$ and $Ni_4(PET)_8$ displayed outstanding electrocatalytic ability for HMFOR. The $Ni_6(PET)_{12}$ exhibited better electrocatalytic ability than $Ni_4(PET)_8$ with higher current density, lower overpotential and faster reaction kinetics. The superior electrochemical ability of $Ni_6(PET)_{12}$ may be due to the enhanced adsorption towards HMF molecule with strong interaction towards hydroxyl group and furan ring. Moreover, it found that the Ni^{2+} species in $Ni_6(PET)_{12}$ could rapidly oxidized into Ni^{3+} species, which could spontaneously capture electron and proton from HMF for oxidation. The theoretical calculation demonstrated that the $Ni_6(PET)_{12}$ process lower free energy barrier than $Ni_4(PET)_8$ to display excellent electrocatalytic performance. This work is of great significance for designing efficient electrocatalysts for HMFOR.

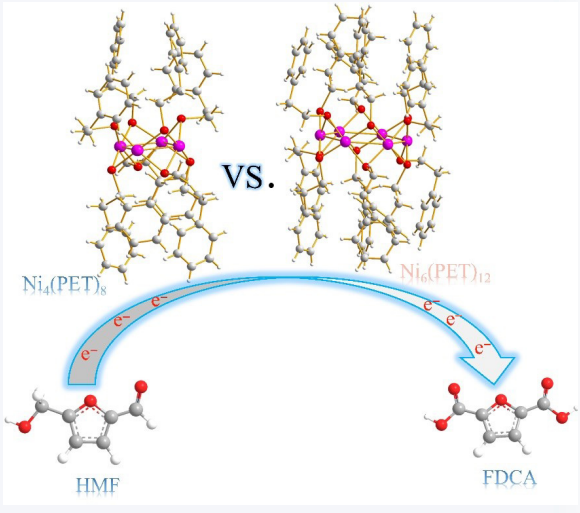

KEYWORDS: atomically precise nickel nanoclusters, 2,5-hydroxymethylfurfural electro-oxidation, Ni^{3+} species

1 Introduction

The energy shortage and environmental degradation caused by the excessive use of non-renewable traditional fossil energy have aroused global concerns [1]. Biomass, which is characterized by wide sources and huge annual output, is a renewable and environmentally friendly carbon source [2]. Recently, 5-hydroxymethylfurfural (HMF) is favored since it is can be oxidized into 2,5-furandicarboxylic acid (FDCA), which is an important monomer to synthesize various fine chemicals, pharmaceutical intermediates and agricultural chemicals [3]. Moreover, FDCA is recognized by the United States Department of Energy as one of the 12 most valuable chemical products in biomass [4, 5]. The traditional HMF oxidation method needs high temperature and toxic oxidant, which pollutes the environment and has huge energy consumption [6]. In the contrast, the electrocatalytic HMF oxidation reaction (HMFOR) is considered to be a green and efficient method due to that it is derived by potential and H_2O [2, 7–9]. Thus, it is key to develop green, efficient and low-cost electrocatalysts for HMFOR.

Nickel sulfide have been considered as one of the most potential electrocatalysts for HMFOR due to their low cost, various morphologies, tunable band gap and unique electronic structure [10, 11]. However, a clear structure–activity relationship at atomic level is difficult to be build due to the polydispersity of sulfide nanoparticles. Fortunately, atomically precise metal nanoclusters (NCs) can provide ideal platform to explore structure–ability relationship and have been widely used in catalysis due to their

Received: June 26, 2024; **Revised:** August 29, 2024
Accepted: August 31, 2024

✉Address correspondence to zhijuanliu@zzu.edu.cn

ultrasmall size, high purity, defined components, precise structure and unique physi-chemical properties [7, 12–18]. Atomically precise metal nanoclusters primarily consist of metal cores, surrounded by organic protective ligands [19]. Thiol (SR) ligands are particularly prevalent in these nanostructures. Within the category of thiol-protected annular clusters, $[Ni(SR)_2]_n$ has been the subject of extensive investigation. The $[Ni(SR)_2]_n$ framework can be interpreted as a cylindrical formation, consisting of n NiS_4 planes that are interconnected by sharing two S vertices, thereby exhibiting a sandwich-like configuration (Fig. S1(a) in the Electronic Supplementary Material (ESM)) [20]. It is noteworthy that all metal atoms are situated within a singular planar arrangement. While S_n rings, consisting of $2n$ S atoms, occupy positions flanking this metal plane on both sides. Additionally, the thiol ligands are systematically disposed on the exterior of the $[Ni_nS_{2n}]$ unit, maintaining a structured and organized layout. With these unique structure, $[Ni(SR)_2]_n$ can be regarded as the ideal model catalysts to reveal the activity origin of Ni-S based nanomaterials in catalysis.

In this work, we have successfully synthesized 2-phenylethanethiol (PET) protected $Ni_6(PET)_{12}$ and $Ni_4(PET)_8$ clusters for HMFOR. Both $Ni_6(PET)_{12}$ and $Ni_4(PET)_8$ clusters are composed of Ni–S bond, where the atomic ratio of Ni^{2+} and S^{2-} is 1:2. The electrochemical results demonstrated that $Ni_6(PET)_{12}$ displayed more excellent electrochemical ability than $Ni_4(PET)_8$ with higher current density and faster reaction kinetics. Moreover, $Ni_6(PET)_{12}$ processes enhanced adsorption towards HMF owing to strong interaction with hydroxyl group and furan ring. According to *in situ* Raman spectra and *ex situ* X-ray photoelectron spectra results, it can be speculated that the Ni^{2+} species in $Ni_6(PET)_{12}$ could be oxidized initially to form Ni^{3+}, which can be worked as active site to capture electron and proton from HMF for oxidation. What is more, the theoretical calculations reveal that $Ni_6(PET)_{12}$ has lower free energy barrier of the rate-determining step (RDS) than $Ni_4(PET)_8$ leading to superior electrocatalytic ability. This work herein provides a valuable guidance for designing efficient electrocatalysts for HMFOR.

2 Experimental section

2.1 Materials and reagents

Nickel(II) acetylacetonate [Ni(acac)$_2$; ($Ni(C_5H_7O_2)_2$), ≥ 95%, Macklin], nickel(II) chloride hexahydrate ($NiCl_2{\cdot}6H_2O$, analytical reagent (AR), Macklin), tetraoctyl-ammonium bromide (TOAB, $[CH_3(CH_2)_7]_4NBr$, 98%, Macklin), L-glutathione (GSH) ($C_{10}H_{17}N_3O_6S$, 99%, Macklin), PET ($C_6H_5CH_2CH_2SH$, ≥ 99%, Macklin), sodium borohydride ($NaBH_4$, ≥ 98.0%, Sigma-Aldrich), toluene (high performance liquid chromatography (HPLC) grade, Fisher Scientific), tetrahydrofuran (THF), dichloromethane (DCM), acetone, methanol and ethanol absolute (AR, Chemical Reagent) were also used as received without further purification.

2.2 Preparation of electrocatalyst

Synthesis of $Ni_6(PET)_{12}$: The synthesis of $Ni_6(PET)_{12}$ nanoclusters refers to the previously reported method [21, 22]. In a typical synthesis, 0.42 mmol of $NiCl_2{\cdot}6H_2O$ and 0.89 mmol of TOAB were dissolved in 100 mL of THF. After that, 2.17 mmol of PET was added to the above solution under stirring, followed by the addition of freshly prepared aqueous $NaBH_4$ (4.23 mmol, 14 mL water) which produced a dark-brown mixture, indicating the formation of Ni NCs. The dark-brown mixture was allowed to stir for 24 h and then concentrated by removing THF using a rotary evaporator. The concentrated product was washed thrice with methanol, centrifuged and then dried overnight in a vacuum drying oven.

Synthesis of $Ni_4(PET)_8$: The synthesis of $Ni_4(PET)_8$ nanoclusters refers to the previously reported method [21, 23]. In a typical synthesis procedure, 0.5 mmol of nickel(II) acetylacetonate and 2.0 mmol of GSH were mixed with 20 mL of acetone in a 40 mL glass vial under vigorous stirring. After 20 min of stirring, the glass vial was cooled to 0 °C using an ice bath. After 20 min, 5 mmol of aqueous $NaBH_4$ (~ 6 mL) as a reducing agent was added rapidly to the cooled reaction mixture under vigorous stirring. After 30 min, the clear acetone supernatant was removed from the glass vial and replaced with 6 mL of water to dissolve the Ni-GSH which was sticking on the glass vial. The obtained 6 mL of the aqueous Ni-GSH complex was mixed with 2 mL of ethanol, 2 mL of toluene and 2 mL of PET in a glass vial heating at 80 °C. The reaction mixture was stirred overnight. After stopping the reaction, the $Ni_4(PET)_8$ cluster was washed three times with methanol to remove the reaction by-products and excess thiols. After washing, it was centrifuged and dried overnight in a vacuum oven.

2.3 Physical characterization

Transmission electron microscopy (TEM, JEM-2100F) was used to study the morphology of the samples. Firstly, $Ni_6(PET)_{12}$ was dissolved in DCM to make a slurry and then the slurry was filtered to form a clear solution. Then a pipette was used to absorb part of the solution and drop it on the copper mesh ultra-thin carbon support film. The powder X-ray diffraction (XRD, D/MAX-3D diffractometer) was characterized crystal structure of the obtained sample. XRD patterns were collected with a Cu Kα source (λ = 0.15406 nm) of Riguku D/Max-2500PC. Ultraviolet–visible (UV–vis) absorption spectra of $Ni_6(PET)_{12}$ and $Ni_4(PET)_8$ were measured over the range 300–800 nm using a U-2000 Spectrophotometer. X-ray photoelectron spectroscopy (XPS) was tested using ESCALAB 250 system (Thermo Fisher Scientific, England) and were used to explore the electronic structure. The Raman spectra were collected on labRAM HR Evolution-HORIBA Raman system. The measurements were performed with a 532 nm laser and the 50× objective lens. The $Ni_6(PET)_{12}$ was tested in the voltage range of 1.1–1.6 V vs. reversible hydrogen electrode (RHE), using a three-electrode system, in which the reference electrode was silver chloride and the counter electrode was platinum foil. The Fourier transform infrared (FTIR) spectra were carried out by a Bruker tensor II spectrometer (BRUKER Co., Bremen, Germany). The test uses an external reflection mode and a three-electrode system, in which the reference electrode is silver chloride and the counter electrode is platinum foil. The reaction conditions were 1 M KOH + 50 mM HMF. First, deduct the background. Then, the *in situ* FTIR spectra of 1.1 – −1.8 V vs. RHE were continuously measured.

2.4 Electrochemical test

All the electrochemical measurements including cyclic voltammetry (CV) and linear sweep voltammetry (LSV) were tested using an electrochemical workstation (CHI760E, CH Instrument) with a three-electrode. The electrocatalyst ink was prepared by dispersing 1 mg catalysts into 500 μL deionized water, 500 μL ethanol and 500 μL 5 wt.% Nafion under sonication for 30 min. The above prepared catalyst solution was dropped on a 1 cm × 1 cm of carbon paper and dried naturally. Carbon rode and saturated calomel

electrode (SCE) were worked as counter electrode and reference electrode, respectively. With electrolyte at 1.0 M KOH and 1.0 M KOH with 50 mM HMF, the LSV curve was recorded at a scan rate of 5 mV·s^{-1} under infrared compensation. All potentials were referenced to a RHE according to the equation $E_{RHE} = E_{SCE} + 0.242 + 0.059 \times pH$ (E_{RHE} represents reversible hydrogen electrode potential and E_{SCE} represents saturated calomel electrode potential). The impedance spectrum was measured at the frequency range from 0.01 Hz to 1000 kHz. All electrocatalytic HMF experiments were carried out at room temperature of 25 °C.

2.5 Product quantification

High performance liquid chromatography (Waters 2695) was used to analyze oxidation products during HMFOR, equipped with ultraviolet–visible detector and a 4.6 mm × 250 mm Ultimate 5 m AQ-C18 column. Mobile phase A (methanol):mobile phase B (5 mM ammonium formate) = 3:7, the flow rate is 0.6 mL·min^{-1}, 265 nm is the wavelength of the UV detector and the separation time is 10 min. Collect 20 μL of electrolyte solution during electrolysis, dilute it to 2 mL with ultrapure water, mix it evenly and inject it into HPLC for test analysis. The HMF conversion rate, FDCA yield and Faraday efficiency (FE) were obtained by the following formulas, respectively

$$\text{HMF conversion}(\%) = [n(\text{HMF consumed})/n(\text{HMF initial})] \times 100 \quad (1)$$

$$\text{FDCA yield}(\%) = [n(\text{FDCA formed})/n(\text{HMF initial})] \times 100 \quad (2)$$

$$\text{FE}(\%) = [n(\text{FDCA formed})/(\text{charge}/6F)] \times 100 \quad (3)$$

where F was the Faraday constant (96,485 C·mol^{-1}) and n was the mol of reactant calculated from the concentration measured by HPLC.

2.6 Theoretical calculation

All the calculations are performed in the framework of the density functional theory (DFT) with the projector augmented plane-wave method, as implemented in the Vienna *ab initio* simulation package [24, 25]. The generalized gradient approximation proposed by Perdew–Burke–Ernzerhof (PBE) is selected for the exchange-correlation potential [26, 27]. The cut-off energy for plane wave is set to 480 eV. The energy criterion is set to 10^{-4} eV in the iterative solution of the Kohn–Sham equation. To avoid interlaminar interactions, a vacuum spacing of 20 Å is applied perpendicular to the slab. The Brillouin zone integration is performed using a 1 × 1 × 1 *k*-mesh. All the structures are relaxed until the residual forces on the atoms have declined to less than 0.05 eV·Å^{-1}. Data analysis and visualization are carried out with the help of VASPKIT [28] code and VESTA [29].

3 Results and discussion

3.1 Characterizations of electrocatalyst

The $Ni_4(PET)_8$ and $Ni_6(PET)_{12}$ clusters were successfully synthesized through a straightforward wet chemical approach. $NiCl_2·6H_2O$ and 2-phenylethyl mercaptan were transformed into the corresponding metal sulfides in the presence of tetraoctylammonium bromide under stirring. After $NaBH_4$-reduction, dark brown mixture could be obtained. The powder XRD technique is a common method to study the crystal structure of samples. As shown in Figs. S1(b) and S1(c) in the ESM, the XRD patterns of $Ni_6(PET)_{12}$ and $Ni_4(PET)_8$ are in good agreement with the simulated patterns, which indicates that the successful synthesis of $Ni_6(PET)_{12}$ and $Ni_4(PET)_8$. It has been previously reported that both $Ni_6(PET)_{12}$ and $Ni_4(PET)_8$ clusters are double-crown-core structures [30–32]. In the $Ni_6(PET)_{12}$ clusters, six nickel atoms form a hexagonal ring. Twelve thiol ligands are positioned above and below the ring, forming SR-Ni-SR bridges (Fig. 1(a)). The spectral characteristics of $Ni_6(PET)_{12}$ and $Ni_4(PET)_8$ were explored by UV–visible absorption spectrum. The strong absorption peaks at ~ 340, 420 and 550 nm were observed, which may be due to the electron transition in the metal core (Fig. 1(b)). Surprisingly, it can be discerned that the peak characteristics of $Ni_4(PET)_8$ exhibit a subtle shift towards shorter wavelengths in comparison to those exhibited by $Ni_6(PET)_{12}$, which is consisted with the previously reported results [21]. The chemical bonds and functional groups of the prepared $Ni_6(PET)_{12}$ and $Ni_4(PET)_8$ were characterized by FTIR infrared spectroscopy. As illustrated in Fig. 1(c), the peak at around 3000 cm^{-1} is associated with the stretching vibration of C–H bond. The peak at 1500–1700 cm^{-1} belongs to the stretching of the aromatic ring. In addition, the peak at ~ 1250 cm^{-1} is attributed to the stretching vibration of C–S. The above peaks reflected in both $Ni_6(PET)_{12}$ and $Ni_4(PET)_8$ clusters indicate that the similar structures of the two clusters. The $Ni_4(PET)_8$ clusters have the similar structure with the $Ni_6(PET)_{12}$ (Fig. 1(d)). XPS is performed to characterize the elemental composition and electronic structure of samples (Fig. S2 in the ESM). The Ni 2p XPS spectrum (Fig. 1(e)) of both $Ni_6(PET)_{12}$ and $Ni_4(PET)_8$ shows peaks at 854.5 and 871.6 eV corresponding to the Ni $2p_{3/2}$ and Ni $2p_{1/2}$ of Ni^{2+} [32–34]. In the S 2p XPS spectrum (Fig. 1(f)), the peaks at 162.6 and 163.8 eV correspond to S $2p_{3/2}$ and S $2p_{1/2}$, respectively, indicating the existence of S^{2-} [34, 35]. As displayed in Fig. S3 in the ESM, the size of the $Ni_6(PET)_{12}$ and $Ni_4(PET)_8$ clusters were examined using TEM. In Fig. S3 in the ESM, the average size of $Ni_6(PET)_{12}$ is about 1.94 nm. Based on the above results, it can be verified the successful preparation of $Ni_6(PET)_{12}$ and $Ni_4(PET)_8$, which could work as ideal model catalyst the reveal the activity origin of HMFOR for Ni-S based nanomaterials.

3.2 Electrochemical test

The electrochemical HMFOR activity of $Ni_6(PET)_{12}$ and $Ni_4(PET)_8$ were explored using a three-electrode system without or with 50 mM HMF in 1 M KOH. The electrochemical oxidation behavior of Ni^{2+}/Ni^{3+} was studied by CV test. The redox pairs are appeared at 1.33–1.42 V, which is attributed to the redox of Ni^{2+}/Ni^{3+} (Fig. S4 in the ESM) [36, 37]. The $Ni_6(PET)_{12}$ displayed much larger redox current density than $Ni_4(PET)_8$ suggesting rich Ni^{2+} content. It can be observed from the CV plots that $Ni_6(PET)_{12}$ exhibits an oxidation peak at 1.39 V [38]. The current density of HMFOR began to increase after the oxidation of Ni^{2+}/Ni^{3+}, indicating that HMFOR over $Ni_6(PET)_{12}$ and $Ni_4(PET)_8$ surface was an indirect oxidation process (Fig. S5 in the ESM). The current density of HMFOR is significantly higher than that of oxygen evolution reaction (OER) at the same overpotential, indicating that HMFOR has a more preferential reaction kinetics. The $Ni_6(PET)_{12}$ exhibits superior HMFOR activity with 1.44 V at 10 mA·cm^{-2}, which is superior to $Ni_4(PET)_8$ (1.66 V) (Fig. 2(a)). It is found in Fig. 2(b) that the current density of $Ni_6(PET)_{12}$ (12.67 mA·cm^{-2}) is about

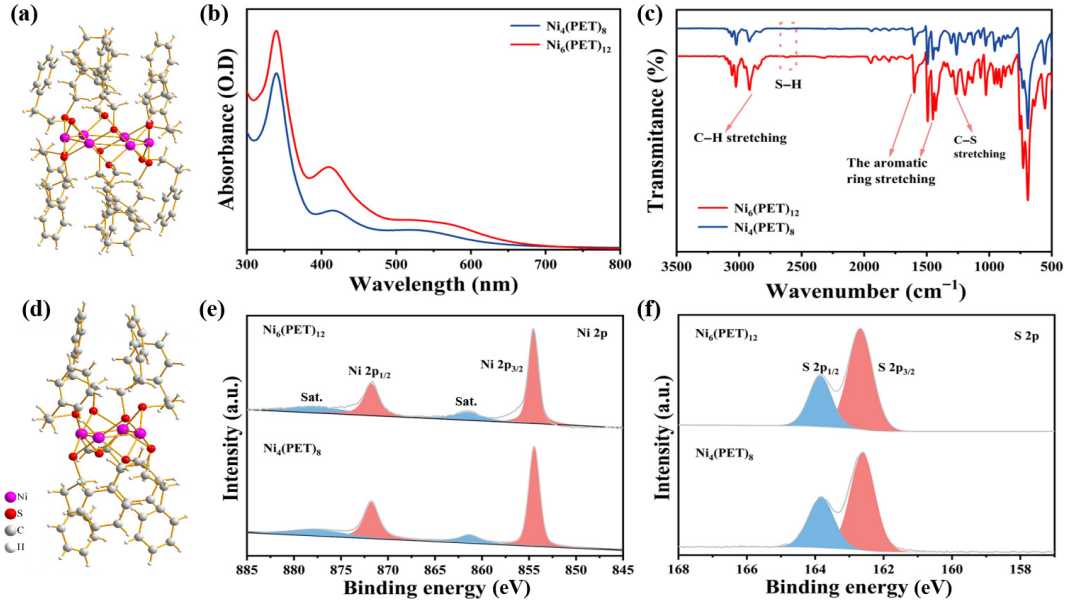

Figure 1 Ball-and-stick view of the crystal structure of the (a) $Ni_6(PET)_{12}$ and (d) $Ni_4(PET)_8$ cluster. (b) The UV–vis (optical density (O.D) means the absorbance of a substance at a wavelength) and (c) FTIR patterns of the $Ni_6(PET)_{12}$ and $Ni_4(PET)_8$. XPS spectra of (e) Ni 2p and (f) S 2p regions in the $Ni_6(PET)_{12}$ and $Ni_4(PET)_8$.

9 times that of $Ni_4(PET)_8$ (1.36 mA·cm^{-2}) at 1.45 V, indicating the superiority of $Ni_6(PET)_{12}$ over $Ni_4(PET)_8$ in HMFOR. The open-circuit potentials (OCP) are tested to reflect the absorb behavior change in the Helmholtz layer of electrocatalysts [39, 40]. When adding 50 mM HMF, the OCP of the electrochemical cell with $Ni_6(PET)_{12}$ was decreased (0.112 V), which is more significantly than that of $Ni_4(PET)_8$ (0.082 V), indicating stronger surface adsorption of HMF on $Ni_6(PET)_{12}$ leading to local rich HMF molecule to participate in HMFOR (Fig. 2(c)). The Tafel slope was calculated to evaluate the reaction kinetics of $Ni_6(PET)_{12}$ and $Ni_4(PET)_8$. Figure 2(d) shows that the Tafel slopes of $Ni_6(PET)_{12}$ of the HMFOR are 44.78 mV·dec^{-1}, which is lower than that of $Ni_4(PET)_8$ (105.64 mV·dec^{-1}), indicating faster reaction kinetics. The Nyquist plots of $Ni_6(PET)_{12}$ and $Ni_4(PET)_8$ at 1.45 V for HMFOR are shown in Fig. 2(e). $Ni_6(PET)_{12}$ displays the smallest semicircle diameter, signifying the smallest charge transfer resistance (R_{ct}) and the fastest reaction kinetics. In order to exclude the effect of exposed active sites on electrochemical ability, the electrochemical abilities of $Ni_4(PET)_8$ and $Ni_6(PET)_{12}$ were normalized by electrochemical active surface areas (ECSAs). The electrochemical double-layer capacitance (C_{dl}) in the non-Faradaic region was recorded. As shown in Fig. S6 in the ESM, the C_{dl} of $Ni_6(PET)_{12}$ and $Ni_4(PET)_8$ are 0.15 and 0.12 mF·cm^{-2}, respectively, indicating that $Ni_6(PET)_{12}$ and $Ni_4(PET)_8$ expose similar number of active sites. After normalized with ECSAs, the $Ni_6(PET)_{12}$ clusters show the best electrochemical capacity, indicating its excellent intrinsic ability (Fig. S7 in the ESM). To explore the adsorption behavior of $Ni_6(PET)_{12}$ cluster towards different functional groups in HMF, LSV tests were carried out in electrolyte with furfuryl alcohol, furfural, benzyl alcohol, benzaldehyde, 5-hydroxyvaleraldehyde and ethanol, respectively (Fig. S8 in the ESM). As shown in Fig. 2(f), the electrochemical activity for hydroxymethyl and aldehyde oxidation of $Ni_6(PET)_{12}$ at 1.45 V was compared. The oxidation current densities of furfuryl alcohol and benzyl alcohol were higher than those of furfural and benzaldehyde indicating that the oxidation of hydroxymethyl was the RDS of HMFOR [41]. In order to compare the effect of the conjugation degree of substrate molecules on the electrocatalytic ability of $Ni_6(PET)_{12}$ cluster, the current densities of benzyl alcohol, furfuryl alcohol and ethanol oxidation at 1.45 V were compared in Fig. 2(g). The results show that the oxidation current densities of benzyl alcohol, furfuryl alcohol and ethanol decrease in turn, indicating that the furan ring may has a great effect on the HMF adsorption for $Ni_6(PET)_{12}$. There are two possible pathways for the oxidation of HMF to FDCA (Fig. S9 in the ESM) [42]. Path 1 is the preferential oxidation of the aldehyde group into the carboxyl group, leading to the formation of intermediate 5-hydroxymethyl-2-furancarboxylic acid (HMFCA) [42, 43]. Path 2 is the oxidation of the hydroxyl group into the aldehyde group, resulting in the formation of 2,5-diformylfuran (DFF) [42, 43]. Both HMFCA and DFF were oxidized to 5-formyl-2-furancarboxylic acid (FFCA) and finally to FDCA [44]. In order to understand the actual HMFOR pathway of $Ni_6(PET)_{12}$, these standard substances were separated by HPLC and the standard curves are shown in Fig. S10 in the ESM. With the increase of electrocatalytic time, the concentration of HMF decreased and the concentration of FDCA increased. In addition, HMFCA and FFCA were also detected in the electrolysis process and almost no DFF was detected, demonstrating that the main pathway of HMF oxidation on $Ni_6(PET)_{12}$ was pathway 1 (Fig. 2(h)). To test the electrochemical stability of $Ni_6(PET)_{12}$, four consecutive potentiostatic cycling tests were carried out. The yield and Faraday efficiency of FDCA on $Ni_6(PET)_{12}$ after 4 electrolysis cycles are higher than 92%, signifying that $Ni_6(PET)_{12}$ clusters have good electrocatalytic performance and excellent stability for HMFOR (Fig. 2(i)). In addition, UV–vis adsorption spectra showed that $Ni_6(PET)_{12}$ maintained the similar characteristic absorption peak after four consecutive electrolysis cycles, indicating its good stability (Fig. S11 in the ESM).

Electrochemical impedance spectroscopy (EIS) is an important way to study the electrode process and interfacial reaction kinetics [45]. The peak at high-frequency region (10^1–10^5 Hz) is related to the internal oxidation of the electrode. The peak at low-frequency region (10^{-1}–10^1 Hz) is related to the non-uniform charge distribution, that is, the appearance of oxidizing substances at the electrode interface [46, 47]. As shown in Figs. 3(a) and 3(b), in 1.10–1.40 V, the phase angle of low frequency region of $Ni_4(PET)_8$

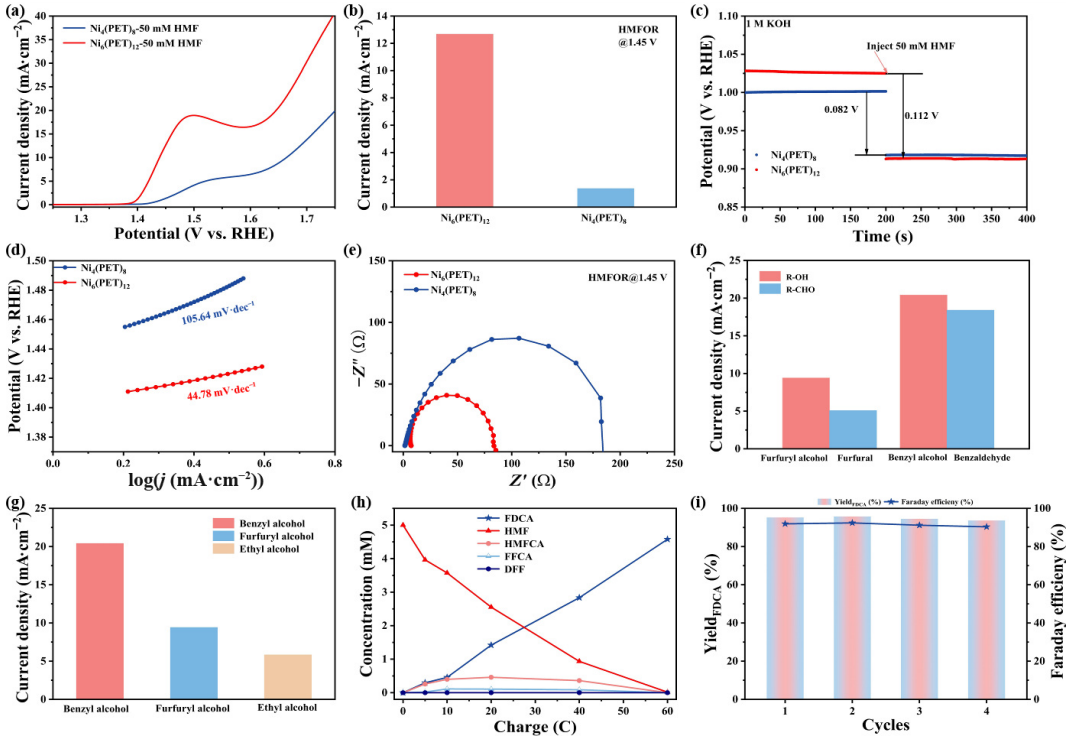

Figure 2 (a) Electrochemical abilities of $Ni_6(PET)_{12}$ and $Ni_4(PET)_8$. (b) Current densities of $Ni_6(PET)_{12}$ and $Ni_4(PET)_8$ at 1.45 V for HMFOR. (c) OCP curves in 1 M KOH with the subsequent adding of 50 mM HMF on $Ni_6(PET)_{12}$ and $Ni_4(PET)_8$ electrode. (d) Tafel slopes and (e) Nyquist plots of $Ni_6(PET)_{12}$ and $Ni_4(PET)_8$ at 1.45 V. (f) Obtained current densities of hydroxymethyl and aldehyde oxidation at $Ni_6(PET)_{12}$ electrode at 1.45 V (this R-OH represents the hydroxyl groups of furfuryl alcohol and benzyl alcohol, and R-CHO represents the aldehyde groups of furfural and benzaldehyde. R means furan ring or phenyl group). (g) Obtained current densities of benzyl alcohol, furfuryl alcohol and ethanol oxidation at $Ni_6(PET)_{12}$ electrode at 1.45 V. (h) Concentration of HMF and its oxidation products under different charges on $Ni_6(PET)_{12}$ during HMFOR. (i) Yield and Faraday efficiency of FDCA on $Ni_6(PET)_{12}$ under four successive electrolysis.

is higher than that of $Ni_6(PET)_{12}$ after the addition of 50 mM HMF, indicating that the kinetics of $Ni_6(PET)_{12}$ for HMFOR process is faster than that of $Ni_4(PET)_8$. In 1 M KOH, a new peak at 1.55 V was found at intermediate frequency region (10^1–10^3 Hz) of $Ni_6(PET)_{12}$ cluster, indicating the occurrence of OER (Fig. S12 in the ESM). The peak at 1.55 V was also found at intermediate frequency region (10^1–10^3 Hz) of $Ni_6(PET)_{12}$ cluster, indicating that the OER process also occurred after the addition of HMF (Fig. 3(b)). After adding HMF, the peak in the low frequency region over $Ni_6(PET)_{12}$ electrode was appeared at 1.40 V indicating the occur of HMFOR. HMFOR occurs after the oxidation of the catalyst itself suggesting the $Ni_6(PET)_{12}$ clusters follow an indirect oxidation mechanism for HMFOR. Ni^{2+} adsorbs *OH initially and loses electrons to form $NiO(OH)_{ads}$ ("ads" means the adsorption state of intermediate products ($NiO(OH)_{ads}$)), which are then reduced to Ni^{2+} by extracting active H atoms from the hydroxyl of HMF [38, 48]. At low potential (1.10–1.35 V), the catalyst undergoes self-oxidation. As the voltage increases to 1.40 V, HMF can react rapidly with $NiO(OH)_{ads}$ produced by the catalyst and the phase angle is greatly reduced in the low frequency region (10^{-1}–10^1 Hz). When the voltage reaches 1.45 and 1.50 V, significant $NiO(OH)_{ads}$ formation occurs. The $NiO(OH)_{ads}$ cannot totally react with HMF, leading to accumulation and electrode passivation. Consequently, the phase angle in the low frequency range (10^{-1}–10^1 Hz) abruptly increases. When the potential was increased to 1.55 V, the competing reaction, OER, began to occur. The *in situ* Bode phase angle diagrams of $Ni_4(PET)_8$ and $Ni_6(PET)_{12}$ in 1 M KOH were also tested for comparation. The equivalent circuit diagram used for fitting is shown in Fig. S13 in the ESM. The corresponding fitting results are summarized in Fig. 3(c) and Tables S1–S3 in the ESM. When in HMF electrolyte, there is an infinite charge transfer resistance (R_{ct}) at low potentials (1.15–1.30 V), indicating that the electrocatalytic reaction has not yet occurred [45]. When the potential is higher than 1.30 V, the sharp decrease of R_{ct} indicates the oxidation of HMF at the electrode interface. When the potential reaches 1.45 and 1.50 V, the R_{ct} began to increase due to electrode passivation. Within the potential range of 1.55 to 1.65 V, the R_{ct} value of $Ni_6(PET)_{12}$ in 1 M KOH remains highly proximate to the R_{ct} value observed after the addition of 50 mM HMF, thereby suggesting that OER begins to predominate within this specific potential window. In Fig. 3(d), the R_{ct} values of $Ni_6(PET)_{12}$ and $Ni_4(PET)_8$ in the HMFOR process are compared. It is found that the R_{ct} value of $Ni_6(PET)_{12}$ is basically lower than that of $Ni_4(PET)_8$, indicating that the $Ni_6(PET)_{12}$ process fast reaction kinetics. As illustrated in Fig. 3(e), OH^- and HMF are adsorbed in the inner layer of $Ni_6(PET)_{12}$ cluster at a low voltage. When the voltage is increased to 1.40 V, HMFOR began to occur coupling with the consumption of OH^- at the interface to form water.

3.3 Mechanism investigation

In order to further explore the chemical state evolution of $Ni_4(PET)_8$ and $Ni_6(PET)_{12}$ clusters during the HMFOR process, *ex situ* XPS was used to analyze the changed valence state of Ni under different voltages (Fig. S14 in the ESM). The relative ratios of Ni^{3+}/Ni^{2+} in $Ni_6(PET)_{12}$ and $Ni_4(PET)_8$ at the different potential were calculated (Figs. 4(a) and 4(b)). In the electrocatalytic HMFOR process of $Ni_6(PET)_{12}$ and $Ni_4(PET)_8$, the Ni^{3+} species were appeared at 1.30 V and the relative content of Ni^{3+}/Ni^{2+} increased sharply at

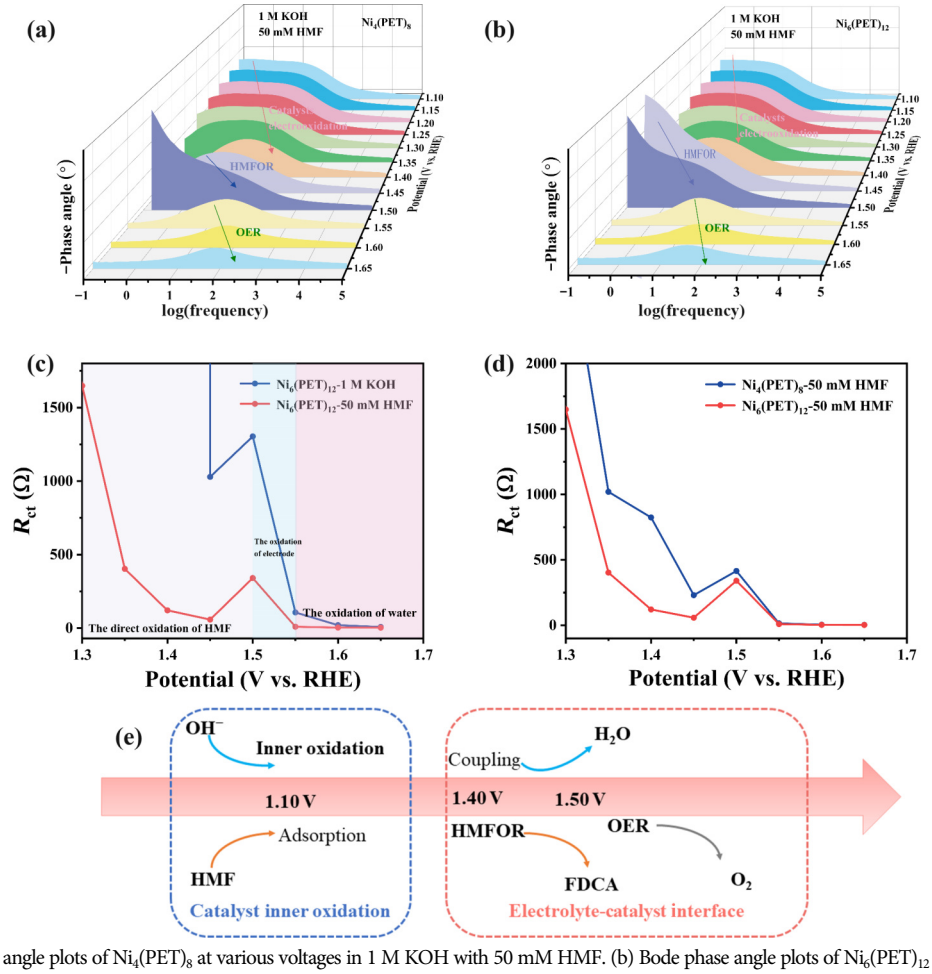

Figure 3 (a) Bode phase angle plots of $Ni_4(PET)_8$ at various voltages in 1 M KOH with 50 mM HMF. (b) Bode phase angle plots of $Ni_6(PET)_{12}$ at various voltages in 1 M KOH with 50 mM HMF. (c) R_{ct} on $Ni_6(PET)_{12}$ in 1 M KOH with and without 50 mM HMF. (d) R_{ct} on $Ni_6(PET)_{12}$ and $Ni_4(PET)_8$. (e) The scheme of the relationship between structure–activity–potential.

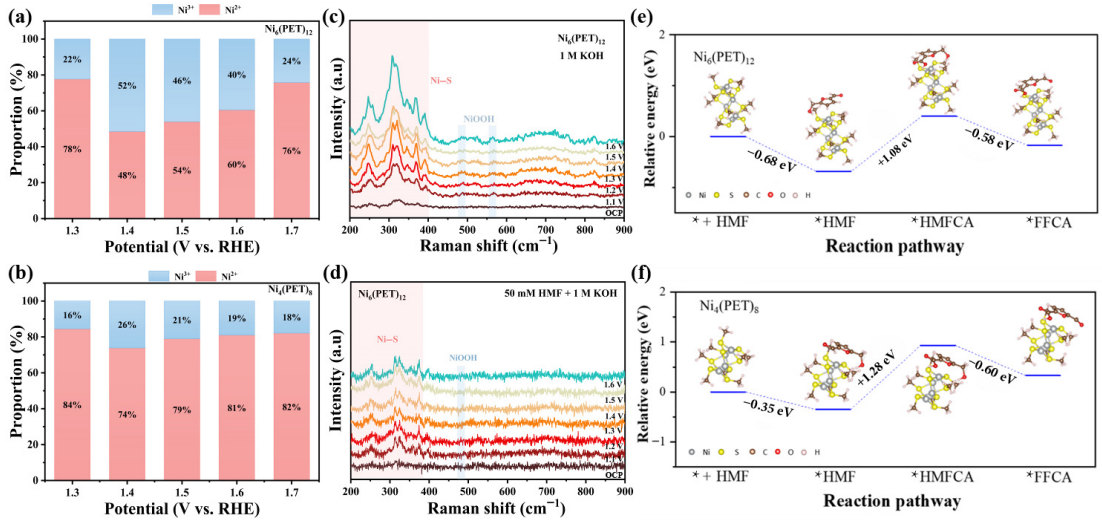

Figure 4 The contents of oxygen species (Ni^{3+}/Ni^{2+}) of (a) $Ni_6(PET)_{12}$ and (b) $Ni_4(PET)_8$ electrode in 1 M KOH with 50 mM HMF at various oxidizing potentials. *In situ* Raman spectroscopy of $Ni_6(PET)_{12}$ for (c) OER and (d) HMFOR. The structural evolution of (e) $Ni_6(PET)_{12}$ and (f) $Ni_4(PET)_8$ in the HMFCA pathway of electrocatalytic HMFOR.

1.40 V suggesting the oxidation of Ni^{2+} species. At 1.40 V, a large amount of Ni^{2+} is oxidized and adsorb OH^- to form $NiO(OH)_{ads}$ with electrophilic oxygen group. Then $NiO(OH)_{ads}$ can capture protons and electrons from HMF to form H_2O, which makes HMF oxidized and Ni^{3+} content decreased. As the voltage continues to increase to 1.60 V, the relative content of Ni^{3+}/Ni^{2+} begins to decrease due to the weakening of metal oxidation kinetics. The number of active Ni^{3+} species generated by the $Ni_6(PET)_{12}$ clusters

in the HMFOR process is higher than that of $Ni_4(PET)_8$, which indicates that the active center of $Ni_6(PET)_{12}$ participating in the catalytic process is significantly increased, thus kinetically accelerating the reaction process. In addition, the relative content of Ni^{3+}/Ni^{2+} does not increase with the increase of potential, indicating that the oxidation of HMF is not a potential-dependent process [49]. Previous literature has reported that SO_4^{2-} adsorbed on the electrode surface can promote the generation of $NiO(OH)_{ads}$ active species and the adsorption of intermediates in HMFOR, which is beneficial to the further improvement of catalytic performance [50]. The valence state analysis of $Ni_6(PET)_{12}$ after HMFOR electrocatalysis at 1.50 V for 8 h showed a peak of Ni^{3+}. At the same time, it is also found that the S^{2-} was oxidized and the peak of SO_4^{2-} appeared (Fig. S15 in the ESM). *In situ* Raman spectroscopy was used to study the electrocatalytic mechanism of the catalyst. In 1 M KOH solution, the peaks at 252, 315 and 368 cm^{-1} belong to the peaks of Ni–S bond (Fig. 4(c)) [50]. In 1 M KOH, the bending and stretching vibration peaks of Ni^{3+}–O at 480 and 560 cm^{-1} can be seen at 1.40 V (Fig. 4(c)), which is due to the electrochemical conversion of Ni^{2+} to NiO(OH) [51–55]. In 1 M KOH with 50 mM HMF solution, the Raman peaks of NiO(OH) are hardly detected, which may be caused that the generated NiO(OH) species are spontaneously and rapidly consumed by HMF (Fig. 4(d)) [56]. *In situ* FTIR technique was used to further explore the reaction pathway of $Ni_6(PET)_{12}$ for HMFOR. As shown in Fig. S16 in the ESM, the band at ~ 1099 cm^{-1} can be attributed to the C=O group on the HMF, indicating that HMF is adsorbed during the HMFOR process [57]. The peak attributed to FFCA at 1567 cm^{-1} becomes increased with the increase of voltage [58]. With the further augment of electrolysis time, the peak directed by FDCA at 1215 cm^{-1} enhances, signifying that the product of FDCA generate [59]. The *in situ* FTIR spectra results are in good agreement with the HPLC results, demonstrating that the reaction process follows path 1. DFT calculations further reveal the reason for the improved catalytic activity of $Ni_6(PET)_{12}$ clusters. The formation of FDCA by electrooxidation of HMF is through a 6-electron transfer pathway. The adsorption configuration and energy distribution of HMFOR on $Ni_6(PET)_{12}$ and $Ni_4(PET)_8$ surfaces were calculated (Figs. 4(e) and 4(f)). It found that the conversion of *HMF to *HMFCA is deemed as RDS for $Ni_6(PET)_{12}$ and $Ni_4(PET)_8$ during HMFOR. The free energy barrier of RDS for $Ni_6(PET)_{12}$ (1.08 eV) is lower than that of $Ni_4(PET)_8$ (1.28 eV) which may be due to the stronger interaction between $Ni_6(PET)_{12}$ and hydroxyl group.

4 Conclusions

In summary, $Ni_6(PET)_{12}$ and $Ni_4(PET)_8$ clusters with 1:2 atomic ratio of Ni^{2+}/S^{2-} have been synthesized and worked as electrocatalysts for HMFOR. It found that the electrochemical HMFOR over both $Ni_6(PET)_{12}$ and $Ni_4(PET)_8$ are indirect oxidation process, where the Ni^{2+} was firstly oxidized into Ni^{3+} species. Then the Ni^{3+} species worked as active site to capture electron and proton of HMF to start the oxidation reaction. It is worth mention that the Ni^{2+} ions in $Ni_6(PET)_{12}$ can be more dramatically oxidized into richer Ni^{3+} to display more excellent electrocatalytic ability than $Ni_4(PET)_8$ with high Faraday efficiency and good electrochemical stability. Moreover, the rection kinetics of $Ni_6(PET)_{12}$ is faster than $Ni_4(PET)_8$. DFT calculations reveal that the free energy barrier of RDS over $Ni_6(PET)_{12}$ electrode is lower than $Ni_4(PET)_8$. This work provides important guidance for the design of efficient catalysts to improve the performance of HMFOR in future.

Electronic Supplementary Material: Supplementary material (experimental methods, XRD, XPS, *in situ* FTIR spectra, TEM images, CV curves, electrochemical curves, and Tables S1–S3) is available in the online version of this article at https://doi.org/10.26599/NR.2025.94907018.

Data availability

All data needed to support the conclusions in the paper are presented in the manuscript and the Electronic Supplementary Material. Additional data related to this paper may be requested from the corresponding author upon request.

Acknowledgements

This work was supported by National Natural Science Foundation of China (No. 22102155) and the China Postdoctoral Science Foundation (Nos. 2021M692909 and 2022T150587).

Declaration of competing interest

All the contributing authors report no conflict of interests in this work.

Author contribution statement

Z. J. L. and Y. Y. W. proposed the research direction and guided the whole experiment. F. W.: Data curation, project administration, validation, writing manuscript, experimental design. L.-Y. L.: Data curation, project administration, validation, experimental design. S.-S. C.: Project administration, writing manuscript. T.-T. L.: Project administration, funding acquisition. X.-M. Y.: Project administration, funding acquisition. All the authors have approved the final manuscript.

Use of AI statement

None.

References

[1] Pan, Y.; Zhang, C.; Lin, Y.; Liu, Z.; Wang, M. M.; Chen, C. Electrocatalyst engineering and structure–activity relationship in hydrogen evolution reaction: From nanostructures to single atoms. *Sci. China Mater.* **2020**, *63*, 921–948.

[2] Yang, M.; Yuan, Z. R.; Peng, R. X.; Wang, S. Y.; Zou, Y. Q. Recent progress on electrocatalytic valorization of biomass-derived organics. *Energy Environ. Mater.* **2022**, *5*, 1117–1138.

[3] Li, Y. W.; Huang, H. T.; Jiang, M. K.; Xi, W. L.; Duan, J. Y.; Ratova, M.; Wu, D. Advancements in transition bimetal catalysts for electrochemical 5-hydroxymethylfurfural (HMF) oxidation. *J. Energy Chem.* **2024**, *98*, 24–46.

[4] Lu, Y. X.; Dong, C. L.; Huang, Y. C.; Zou, Y. Q.; Liu, Y. B.; Li, Y. Y.; Zhang, N. N.; Chen, W.; Zhou, L.; Lin, H. Z. et al. Hierarchically nanostructured NiO-CO_3O_4 with rich interface defects for the electro-oxidation of 5-hydroxymethylfurfural. *Sci. China Chem.* **2020**, *63*, 980–986.

[5] Zhou, S. H.; Dai, F. L.; Xiang, Z. Y.; Song, T.; Liu, D. T.; Lu, F. C.; Qi, H. S. Zirconium-lignosulfonate polyphenolic polymer for highly efficient hydrogen transfer of biomass-derived oxygenates under mild conditions. *Appl. Catal. B: Environ.* **2019**, *248*, 31–43.

[6] Chen, C. L.; Wang, L. C.; Zhu, B.; Zhou, Z. Q.; El-Hout, S. I.; Yang, J.; Zhang, J. 2,5-Furandicarboxylic acid production via catalytic

oxidation of 5-hydroxymethylfurfural: Catalysts, processes and reaction mechanism. *J. Energy Chem.* **2021**, *54*, 528–554.

[7] Tang, C.; Zheng, Y.; Jaroniec, M.; Qiao, S. Z. Electrocatalytic refinery for sustainable production of fuels and chemicals. *Angew. Chem., Int. Ed.* **2021**, *60*, 19572–19590.

[8] Jin, J.; Fang, Y. Y.; Zhang, T. Y.; Han, A. J.; Wang, B. Q.; Liu, J. F. Ultrasmall Ag nanoclusters anchored on NiCo-layered double hydroxide nanoarray for efficient electrooxidation of 5-hydroxymethylfurfural. *Sci. China Mater.* **2022**, *65*, 2704–2710.

[9] Yang, Y. C.; Mu, T. C. Electrochemical oxidation of biomass derived 5-hydroxymethylfurfural (HMF): Pathway, mechanism, catalysts and coupling reactions. *Green Chem.* **2021**, *23*, 4228–4254.

[10] Zhang, R.; Gao, F.; Yang, C.; Bian, Y.; Wang, G.; Xue, K.; Zhang, J.; Wang, C.; Gao, X. Boosting hydrogen evolution via anodic oxidation of 5-hydroxymethylfurfural in anion exchange membrane electrolyzer over a metallic heterostructure. *Mater. Today Nano* **2023**, *23*, 100373.

[11] Li, S. Q.; Wang, S. B.; Wang, Y. H.; He, J. H.; Li, K.; Xu, Y. J.; Wang, M. X.; Zhao, S. Y.; Li, X. N.; Zhong, X. et al. Doped Mn enhanced NiS electrooxidation performance of HMF into FDCA at industrial-level current density. *Adv. Funct. Mater.* **2023**, *33*, 2214488.

[12] Wu, Z. K.; Jin, R. C. Stability of the two Au–S binding modes in $Au_{25}(SG)_{18}$ nanoclusters probed by NMR and optical spectroscopy. *ACS Nano* **2009**, *3*, 2036–2042.

[13] Galchenko, M.; Black, A.; Heymann, L.; Klinke, C. Field effect and photoconduction in Au_{25} nanoclusters films. *Adv. Mater.* **2019**, *31*, 1900684.

[14] Antonello, S.; Perera, N. V.; Ruzzi, M.; Gascón, J. A.; Maran, F. Interplay of charge state, lability, and magnetism in the molecule-like $Au_{25}(SR)_{18}$ cluster. *J. Am. Chem. Soc.* **2013**, *135*, 15585–15594.

[15] Du, Y. X.; Sheng, H. T.; Astruc, D.; Zhu, M. Z. Atomically precise noble metal nanoclusters as efficient catalysts: A bridge between structure and properties. *Chem. Rev.* **2020**, *120*, 526–622.

[16] Jia, T. T.; Yang, G.; Mo, S. J.; Wang, Z. Y.; Li, B. J.; Ma, W.; Guo, Y. X.; Chen, X. Y.; Zhao, X. L.; Liu, J. Q. et al. Atomically precise gold-levonorgestrel nanocluster as a radiosensitizer for enhanced cancer therapy. *ACS Nano* **2019**, *13*, 8320–8328.

[17] Song, X. R.; Goswami, N.; Yang, H. H.; Xie, J. P. Functionalization of metal nanoclusters for biomedical applications. *Analyst* **2016**, *141*, 3126–3140.

[18] Yao, Q. F.; Chen, T. K.; Yuan, X.; Xie, J. P. Toward total synthesis of thiolate-protected metal nanoclusters. *Acc. Chem. Res.* **2018**, *51*, 1338–1348.

[19] Li, S.; Li, N. N.; Dong, X. Y.; Zang, S. Q.; Mak, T. C. W. Chemical flexibility of atomically precise metal clusters. *Chem. Rev.* **2024**, *124*, 7262–7378.

[20] Kauffman, D. R.; Alfonso, D.; Tafen, D. N.; Lekse, J.; Wang, C. J.; Deng, X. Y.; Lee, J.; Jang, H.; Lee, J. S.; Kumar, S. et al. Electrocatalytic oxygen evolution with an atomically precise nickel catalyst. *ACS Catal.* **2016**, *6*, 1225–1234.

[21] Joya, K. S.; Sinatra, L.; AbdulHalim, L. G.; Joshi, C. P.; Hedhili, M. N.; Bakr, O. M.; Hussain, I. Atomically monodisperse nickel nanoclusters as highly active electrocatalysts for water oxidation. *Nanoscale* **2016**, *8*, 9695–9703.

[22] Kagalwala, H. N.; Gottlieb, E.; Li, G.; Li, T.; Jin, R. C.; Bernhard, S. Photocatalytic hydrogen generation system using a nickel-thiolate hexameric cluster. *Inorg. Chem.* **2013**, *52*, 9094–9101.

[23] Qian, H. F.; Zhu, Y.; Jin, R. C. Size-focusing synthesis, optical and electrochemical properties of monodisperse $Au_{38}(SC_2H_4Ph)_{24}$ nanoclusters. *ACS Nano* **2009**, *3*, 3795–3803.

[24] Kresse, G.; Hafner, J. *Ab initio* molecular dynamics for open-shell transition metals. *Phys. Rev. B* **1993**, *48*, 13115–13118.

[25] Kresse, G.; Furthmüller, J. Efficient iterative schemes for *ab initio* total-energy calculations using a plane-wave basis set. *Phys. Rev. B* **1996**, *54*, 11169–11186.

[26] Perdew, J. P.; Burke, K.; Ernzerhof, M. Generalized gradient approximation made simple. *Phys. Rev. Lett.* **1996**, *77*, 3865–3868.

[27] Kohn, W.; Sham, L. J. Self-consistent equations including exchange and correlation effects. *Phys. Rev.* **1965**, *140*, A1133–A1138.

[28] Wang, V.; Xu, N.; Liu, J. C.; Tang, G.; Geng, W. T. VASPKIT: A user-friendly interface facilitating high-throughput computing and analysis using VASP code. *Comput. Phys. Commun.* **2021**, *267*, 108033.

[29] Momma, K.; Izumi, F. *VESTA*: A three-dimensional visualization system for electronic and structural analysis. *J. Appl. Crystallogr.* **2008**, *41*, 653–658.

[30] Hu, W. G.; Sun, Y. N.; Li, S. H.; Cheng, X. L.; Cai, X.; Chen, M. Y.; Zhu, Y. Visible-light-driven methane conversion with oxygen enabled by atomically precise nickel catalyst. *CCS Chem.* **2021**, *3*, 2509–2519.

[31] Cheng, X. L.; Chai, X. Q.; Hu, W. G.; Li, S. G.; Zhu, Y. The on-and-off dynamics of thiophene on a nickel cluster enables efficient hydrodesulfurization and excellent stability at high temperatures. *Nanoscale* **2019**, *11*, 4369–4375.

[32] Billo, T.; Fu, F. Y.; Raghunath, P.; Shown, I.; Chen, W. F.; Lien, H. T.; Shen, T. H.; Lee, J. F.; Chan, T. S.; Huang, K. Y. et al. Ni-nanocluster modified black TiO_2 with dual active sites for selective photocatalytic CO_2 reduction. *Small* **2018**, *14*, 1702928.

[33] Qian, L.; Gu, L.; Yang, L.; Yuan, H. Y.; Xiao, D. Direct growth of $NiCO_2O_4$ nanostructures on conductive substrates with enhanced electrocatalytic activity and stability for methanol oxidation. *Nanoscale* **2013**, *5*, 7388–7396.

[34] Wei, J. D.; Zhao, R. Q.; Luo, D.; Lu, X. Y.; Dong, W. X.; Huang, Y. C.; Cheng, X. M.; Ni, Y. H. Atomically precise $Ni_6(SC_2H_4Ph)_{12}$ nanoclusters on graphitic carbon nitride nanosheets for boosting photocatalytic hydrogen evolution. *J. Colloid Interface Sci.* **2023**, *631*, 212–221.

[35] Liu, C. F.; Shi, X. R.; Yue, K. H.; Wang, P. J.; Zhan, K.; Wang, X. Y.; Xia, B. Y.; Yan, Y. S-species-evoked high-valence $Ni^{2+\delta}$ of the evolved β-$Ni(OH)_2$ electrode for selective oxidation of 5-hydroxymethylfurfural. *Adv. Mater.* **2023**, *35*, 2211177.

[36] Zhang, J.; Zhang, Q. Y.; Feng, X. L. Support and interface effects in water-splitting electrocatalysts. *Adv. Mater.* **2019**, *31*, 1808167.

[37] Zhou, B.; Li, Y. Y.; Zou, Y. Q.; Chen, W.; Zhou, W.; Song, M. L.; Wu, Y. J.; Lu, Y. X.; Liu, J. L.; Wang, Y. Y. et al. Platinum modulates redox properties and 5-hydroxymethylfurfural adsorption kinetics of $Ni(OH)_2$ for biomass upgrading. *Angew. Chem., Int. Ed.* **2021**, *60*, 22908–22914.

[38] Taitt, B. J.; Nam, D. H.; Choi, K. S. A comparative study of nickel, cobalt, and iron oxyhydroxide anodes for the electrochemical oxidation of 5-hydroxymethylfurfural to 2,5-furandicarboxylic acid. *ACS Catal.* **2019**, *9*, 660–670.

[39] Zhou, P.; Lv, X. S.; Tao, S. S.; Wu, J. C.; Wang, H. F.; Wei, X. X.; Wang, T. H.; Zhou, B.; Lu, Y. X.; Frauenheim, T. et al. Heterogeneous-interface-enhanced adsorption of organic and hydroxyl for biomass electrooxidation. *Adv. Mater.* **2022**, *34*, 2204089.

[40] Heidary, N.; Kornienko, N. Electrochemical biomass valorization on gold-metal oxide nanoscale heterojunctions enables investigation of both catalyst and reaction dynamics with *operando* surface-enhanced Raman spectroscopy. *Chem. Sci.* **2020**, *11*, 1798–1806.

[41] Zhang, N. N.; Zou, Y. Q.; Tao, L.; Chen, W.; Zhou, L.; Liu, Z. J.; Zhou, B.; Huang, G.; Lin, H. Z.; Wang, S. Y. Electrochemical oxidation of 5-hydroxymethylfurfural on nickel nitride/carbon nanosheets: Reaction pathway determined by *in situ* sum frequency generation vibrational spectroscopy. *Angew. Chem., Int. Ed.* **2019**, *58*, 15895–15903.

[42] Lin, R.; Salehi, M.; Guo, J. X.; Seifitokaldani, A. High oxidation state enabled by plated Ni-P achieves superior electrocatalytic performance

for 5-hydroxymethylfurfural oxidation reaction. *iScience* **2022**, *25*, 104744.

[43] Lu, Y. X.; Liu, T. Y.; Dong, C. L.; Yang, C. M.; Zhou, L.; Huang, Y. C.; Li, Y. F.; Zhou, B.; Zou, Y. Q.; Wang, S. Y. Tailoring competitive adsorption sites by oxygen-vacancy on cobalt oxides to enhance the electrooxidation of biomass. *Adv. Mater.* **2022**, *34*, 2107185.

[44] You, B.; Liu, X.; Jiang, N.; Sun, Y. J. A general strategy for decoupled hydrogen production from water splitting by integrating oxidative biomass valorization. *J. Am. Chem. Soc.* **2016**, *138*, 13639–13646.

[45] Bredar, A. R. C.; Chown, A. L.; Burton, A. R.; Farnum, B. H. Electrochemical impedance spectroscopy of metal oxide electrodes for energy applications. *ACS Appl. Energy Mater.* **2020**, *3*, 66–98.

[46] Chen, W.; Xu, L. T.; Zhu, X. R.; Huang, Y. C.; Zhou, W.; Wang, D. D.; Zhou, Y. Y.; Du, S. Q.; Li, Q. L.; Xie, C. et al. Unveiling the electrooxidation of urea: Intramolecular coupling of the N–N bond. *Angew. Chem., Int. Ed.* **2021**, *60*, 7297–7307.

[47] Lu, Y. X.; Dong, C. L.; Huang, Y. C.; Zou, Y. Q.; Liu, Z. J.; Liu, Y. B.; Li, Y. Y.; He, N. H.; Shi, J. Q.; Wang, S. Y. Identifying the geometric site dependence of spinel oxides for the electrooxidation of 5-hydroxymethylfurfural. *Angew. Chem., Int. Ed.* **2020**, *59*, 19215–19221.

[48] Chen, W.; Xie, C.; Wang, Y. Y.; Zou, Y. Q.; Dong, C. L.; Huang, Y. C.; Xiao, Z. H.; Wei, Z. X.; Du, S. Q.; Chen, C. et al. Activity origins and design principles of nickel-based catalysts for nucleophile electrooxidation. *Chem* **2020**, *6*, 2974–2993.

[49] Lu, Y. X.; Liu, T. Y.; Huang, Y. C.; Zhou, L.; Li, Y. Y.; Chen, W.; Yang, L.; Zhou, B.; Wu, Y. D.; Kong, Z. J. et al. Integrated catalytic sites for highly efficient electrochemical oxidation of the aldehyde and hydroxyl groups in 5-hydroxymethylfurfural. *ACS Catal.* **2022**, *12*, 4242–4251.

[50] Xiao, D. F.; Bao, X. L.; Dai, D. J.; Gao, Y. G.; Si, S. H.; Wang, Z. Y.; Liu, Y. Y.; Wang, P.; Zheng, Z. K.; Cheng, H. F. et al. Boosting the electrochemical 5-hydroxymethylfurfural oxidation by balancing the competitive adsorption of organic and OH^- over controllable reconstructed Ni_3S_2/NiO_x. *Adv. Mater.* **2023**, *35*, 2304133.

[51] Zhang, P. L.; Sheng, X.; Chen, X. Y.; Fang, Z. Y.; Jiang, J.; Wang, M.; Li, F. S.; Fan, L. Z.; Ren, Y. S.; Zhang, B. B. et al. Paired electrocatalytic oxygenation and hydrogenation of organic substrates with water as the oxygen and hydrogen source. *Angew. Chem., Int. Ed.* **2019**, *58*, 9155–9159.

[52] Huang, C. Q.; Huang, Y.; Liu, C. B.; Yu, Y. F.; Zhang, B. Integrating hydrogen production with aqueous selective semi-dehydrogenation of tetrahydroisoquinolines over a Ni_2P bifunctional electrode. *Angew. Chem., Int. Ed.* **2019**, *58*, 12014–12017.

[53] Deng, X. H.; Li, M.; Fan, Y.; Wang, L.; Fu, X. Z.; Luo, J. L. Constructing multifunctional "nanoplatelet-on-nanoarray" electrocatalyst with unprecedented activity towards novel selective organic oxidation reactions to boost hydrogen production. *Appl. Catal. B: Environ.* **2020**, *278*, 119339.

[54] Liu, X. P.; Wang, R.; Wei, M. Y.; Wang, X. H.; Qiu, J. Y.; Zhang, J. R.; Li, S. L.; Chen, Y. Cross-linked α-$Ni(OH)_2$ nanosheets with a Ni^{3+}-rich structure for accelerating electrochemical oxidation of 5-hydroxymethylfurfural. *J. Colloid Interface Sci.* **2024**, *657*, 438–448.

[55] Zhang, X.; Su, H.; Cui, P. X.; Cao, Y. Y.; Teng, Z. Y.; Zhang, Q. T.; Wang, Y.; Feng, Y. B.; Feng, R.; Hou, J. X. et al. Developing Ni single-atom sites in carbon nitride for efficient photocatalytic H_2O_2 production. *Nat. Commun.* **2023**, *14*, 7115.

[56] Zhou, Z. Y.; Xie, Y. N.; Sun, L. Z.; Wang, Z. M.; Wang, W. K.; Jiang, L. Z.; Tao, X.; Li, L. N.; Li, X. H.; Zhao, G. H. Strain-induced *in situ* formation of NiOOH species on Co–Co bond for selective electrooxidation of 5-hydroxymethylfurfural and efficient hydrogen production. *Appl. Catal. B: Environ.* **2022**, *305*, 121072.

[57] Zeng, L. Y.; Chen, Y. J.; Sun, M. Z.; Huang, Q. Z.; Sun, K. A.; Ma, J. Y.; Li, J.; Tan, H.; Li, M. G.; Pan, Y. et al. Cooperative Rh-O_5/Ni(Fe) site for efficient biomass upgrading coupled with H_2 production. *J. Am. Chem. Soc.* **2023**, *145*, 17577–17587.

[58] Wu, J. C.; Kong, Z. J.; Li, Y. Y.; Lu, Y. X.; Zhou, P.; Wang, H. F.; Xu, L. T.; Wang, S. Y.; Zou, Y. Q. Unveiling the adsorption behavior and redox properties of PtNi nanowire for biomass-derived molecules electrooxidation. *ACS Nano* **2022**, *16*, 21518–21526.

[59] Lu, L. Y.; Wen, C. Y.; Wang, H. Y.; Li, Y. H.; Wu, J. C.; Wang, C. G. Tailoring the electron structure and substrate adsorption energy of Ni hydroxide via Co doping to enhance the electrooxidation of biomass-derived chemicals. *J. Catal.* **2023**, *424*, 1–8.